
Using Artificial Intelligence to Model Phase Changes in the Mantle

Preliminary Draft

Buchanan Kerswell



04 July 2023

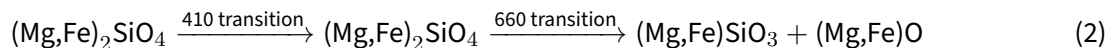
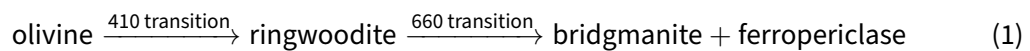
Contents

1	Introduction	2
1.1	Mantle Transition Zones	2
1.2	Current Limitations	2
1.3	Hypothesis Statement	3
2	Computing a Database of Mineral Assemblages and Rock Properties in the Mantle	4
2.1	PT Conditions in the Upper Mantle	4
2.2	Bulk Composition of the Upper Mantle	4
3	References	5
4	Appendix	7
4.1	Gibbs Free Energy Minimization Benchmarking Results	7
5	Extra	8

1 Introduction

1.1 Mantle Transition Zones

The dominant mineral phases in Earth's mantle are olivine, ringwoodite, bridgmanite, and ferropericlase (Ringwood, 1991; Ringwood, 1975). Depending on the assumed mantle composition (e.g., Green, 1979; Jagoutz et al., 1979; Ringwood, 1962; Sun, 1982), these four phases alone may comprise up to 60–90% of the mantle (Stixrude & Lithgow-Bertelloni, 2012). Work since the 1950's has established that a series of discrete phase changes near 410 km and 660 km depth (Equation 1) define critical mantle transition zones (MTZs) where physical properties of the mantle abruptly change (e.g, density, elasticity, etc., Ishii et al., 2018; Ita & Stixrude, 1992; Ito & Takahashi, 1989). While the physio-chemical nature of MTZs are continuously under investigation (Fei et al., 2017; Goes et al., 2022; Kiseeva et al., 2018; Pearson et al., 2014; Waszek et al., 2021; Yoshino et al., 2008; Zhou et al., 2022), it is widely accepted that mantle convection, melting, and plate tectonics are strongly impacted by MTZs (Fukao et al., 2001; Karato et al., 2001; Kuritani et al., 2019; Li et al., 2019; Ringwood, 1991; Schubert et al., 1975; Wang et al., 2015; Yang & Faccenda, 2020). Thus, numerical geodynamic models that lack MTZs are only limited first-order approximations of mantle convection, melting, and plate tectonics.



1.2 Current Limitations

Even with the simplest parameterizations, however, full coupling of pressure-temperature-composition-time (PTXt)-dependent phase changes with large-scale geodynamic models has been intractable because current Gibbs free energy minimization programs (GFEMs, Connolly, 2009; Riel et al., 2022) are slow to converge on stable solutions. For example, it could take more than 75 hours to compute phase transitions for a single timestep during a geodynamic simulation—assuming a 2D mesh resolution of 900x300 and a 1-second computation time for GFEM at each node (see Figure 1 and Table 2). Although recent work to parallelize GFEM (Riel et al., 2022) has increased GFEM efficiency dramatically (Figure 1), directly coupling GFEM algorithms to geodynamic codes requires GFEM efficiency on the order of milliseconds to be feasible, or alternatively, applying parallelization to thousands of cores. This rate of improvement seems unlikely within the current GFEM paradigm and gaining access to many GPUs or thousands of CPU cores is inaccessible in many cases.

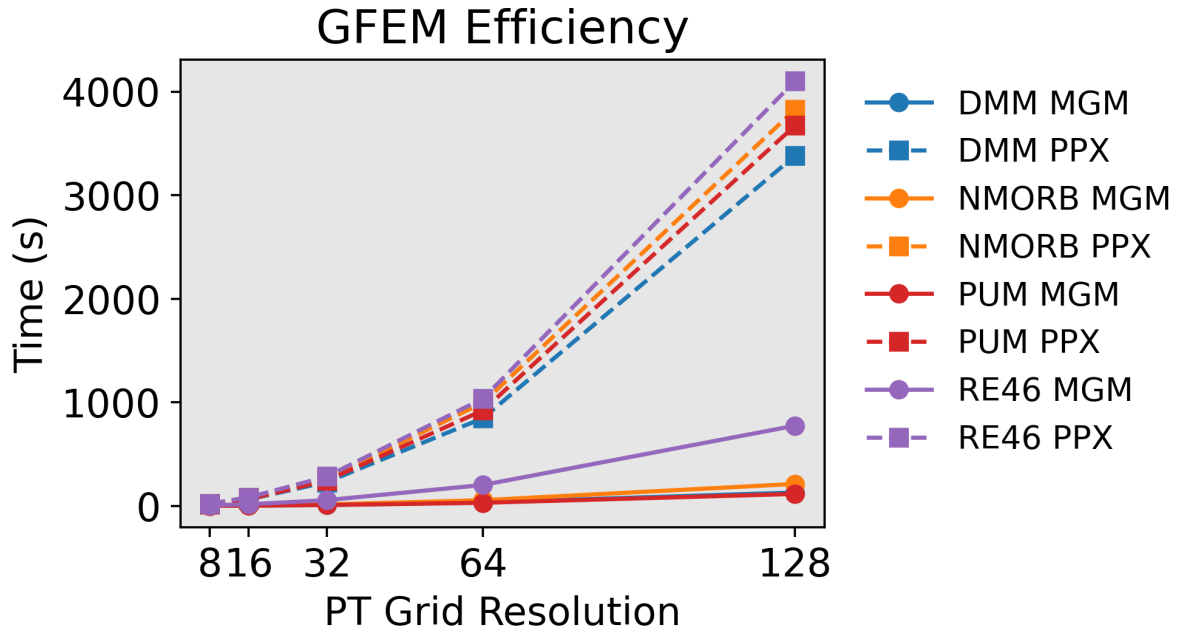


Figure 1: Benchmark results for programs MAGEMin and Perple_X. Note that MAGEMin was ran in parallel on 6 CPU cores, while Perple_X has no parallel capabilities. In the best case, GFEM takes 124 seconds (see Table 2 in Appendix 4.1).

1.3 Hypothesis Statement

To overcome the intractability of coupling PTXt-dependent phase changes with large-scale geodynamic simulations, we propose a novel approach to inferring PTXt-dependent phase changes using machine learning (ML). We hypothesize that pre-trained neural networks can improve efficiency by up to 3 orders of magnitude vs. GFEM for predicting PTXt-dependent phase changes in the mantle. If true, directly coupling PTXt-dependent phase changes with large-scale geodynamic simulations will be feasible—enabling new insights into tectonic plates and mantle plume interactions near MTZs. Moreover, training neural networks is generalizable to other datasets, thus demonstrating success in our proposed use-case has potential for adoption to other computationally-intensive models of Earth processes in the atmosphere, hydrosphere, biosphere and geosphere. If false, however, new paradigms for directly coupling PTXt-dependent phase changes with large-scale geodynamic simulations will need to be reconsidered.

2 Computing a Database of Mineral Assemblages and Rock Properties in the Mantle

2.1 PT Conditions in the Upper Mantle

High-pressure experiments conducted since the 1990s demonstrate the reaction ringwoodite \leftrightarrow bridgmanite + ferropericlasite occurs at pressures coinciding with the 660 km discontinuity in the upper mantle (23.4 ± 0.05 GPa) and 1900–2000 K (Ishii et al., 2018; Ito & Katsura, 1989; Ito & Takahashi, 1989). Our MAD training datasets are thus computed across 1.0–24.0 GPa (10–240 kbar) and 773–2273 K (500–2000 °C). This PT range encompasses expected mantle transition PTs, as well as conditions that occur in subduction zone and mantle-plume settings (???cite).

2.2 Bulk Composition of the Upper Mantle

Table 1: Estimated bulk compositions (in wt. % oxides) for the mantle.

Sample	SiO ₂	Al ₂ O ₃	CaO	MgO	FeO	K ₂ O	Na ₂ O	TiO ₂	O ₂	Cr ₂ O ₃	Reference
PUM	44.90	4.44	3.54	37.71	8.03	0.029	0.36	0.20	0.01	0.38	Sun & McDonough (1989)
DMM	44.71	3.98	3.17	38.73	8.18	0.006	0.13	0.13	0.01	0.57	Workman & Hart (2005)
RE46	50.72	9.16	15.21	16.25	7.06	0.010	1.47	0.39	0.35	0.01	Yang et al. (1996)
NMORB	53.21	9.41	12.21	12.21	8.65	0.090	2.90	1.21	0.69	0.02	Gale et al. (2013)

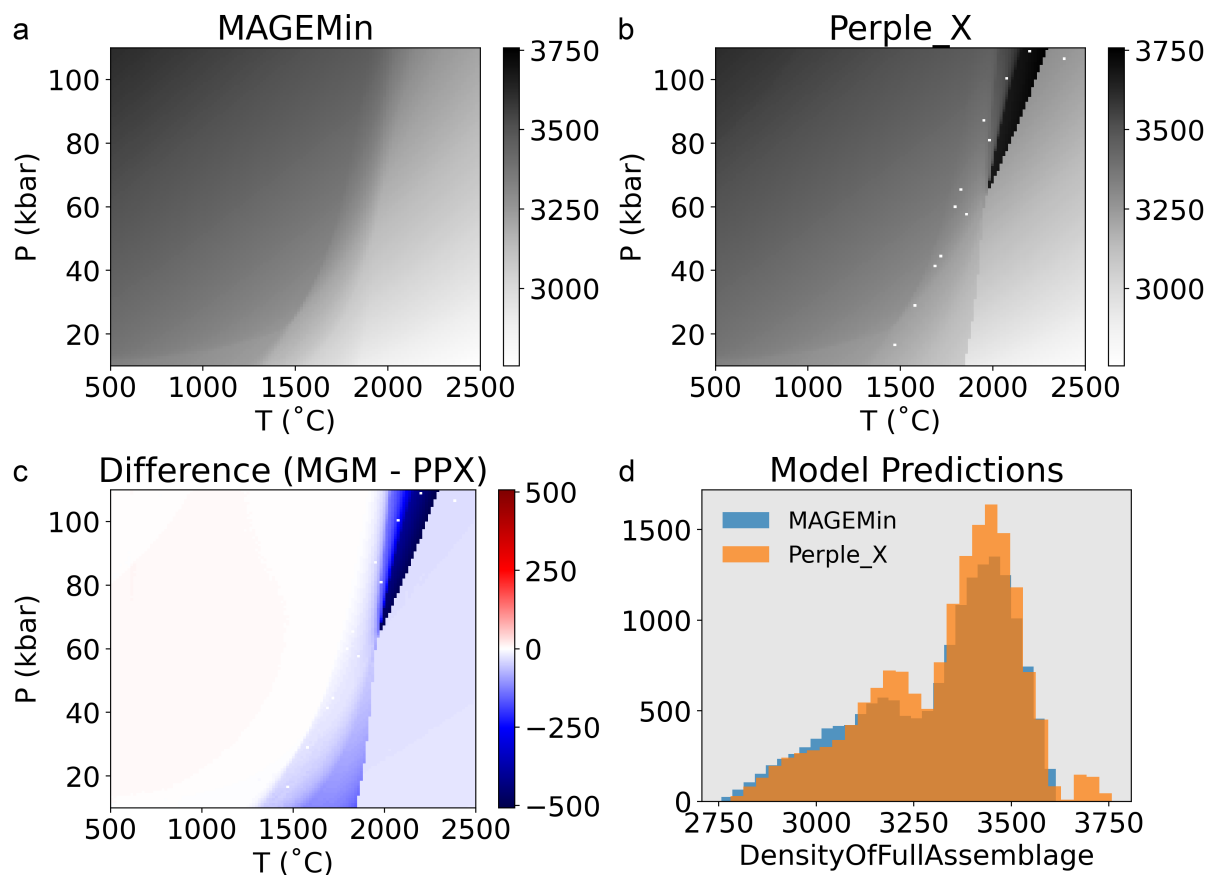


Figure 2: caption

3 References

- Connolly, J. (2009). The geodynamic equation of state: What and how. *Geochemistry, Geophysics, Geosystems*, 10(10).
- Fei, H., Yamazaki, D., Sakurai, M., Miyajima, N., Ohfuji, H., Katsura, T., & Yamamoto, T. (2017). A nearly water-saturated mantle transition zone inferred from mineral viscosity. *Science Advances*, 3(6), e1603024.
- Fukao, Y., Widiyantoro, S., & Obayashi, M. (2001). Stagnant slabs in the upper and lower mantle transition region. *Reviews of Geophysics*, 39(3), 291–323.
- Gale, A., Dalton, C., Langmuir, C., Su, Y., & Schilling, J. (2013). The mean composition of ocean ridge basalts. *Geochemistry, Geophysics, Geosystems*, 14(3), 489–518.
- Goes, S., Yu, C., Ballmer, M., Yan, J., & Hilst, R. van der. (2022). Compositional heterogeneity in the mantle transition zone. *Nature Reviews Earth & Environment*, 3(8), 533–550.
- Green, D. (1979). Petrogenesis of mid ocean ridge basalts. *The Earth: Its Origin, Structure and Evolution*,

200–299.

- Ishii, T., Huang, R., Fei, H., Koemets, I., Liu, Z., Maeda, F., et al. (2018). Complete agreement of the post-spinel transition with the 660-km seismic discontinuity. *Scientific Reports*, 8(1), 6358.
- Ita, J., & Stixrude, L. (1992). Petrology, elasticity, and composition of the mantle transition zone. *Journal of Geophysical Research: Solid Earth*, 97(B5), 6849–6866.
- Ito, E., & Katsura, T. (1989). A temperature profile of the mantle transition zone. *Geophysical Research Letters*, 16(5), 425–428.
- Ito, E., & Takahashi, E. (1989). Postspinel transformations in the system $\text{Mg}_2\text{SiO}_4\text{-Fe}_2\text{SiO}_4$ and some geophysical implications. *Journal of Geophysical Research: Solid Earth*, 94(B8), 10637–10646.
- Jagoutz, E., Palme, H., Baddenhausen, H., Blum, K., Cendales, M., Dreibus, G., et al. (1979). The abundances of major, minor and trace elements in the earth's mantle as derived from primitive ultramafic nodules. In *Lunar and planetary science conference, 10th, houston, tex., march 19-23, 1979, proceedings. Volume 2.(A80-23617 08-91) new york, pergamon press, inc., 1979, p. 2031-2050. Research supported by the deutsche forschungsgemeinschaft.* (Vol. 10, pp. 2031–2050).
- Karato, S., Riedel, M., & Yuen, D. (2001). Rheological structure and deformation of subducted slabs in the mantle transition zone: Implications for mantle circulation and deep earthquakes. *Physics of the Earth and Planetary Interiors*, 127(1-4), 83–108.
- Kiseeva, E., Vasiukov, D., Wood, B., McCammon, C., Stachel, T., Bykov, M., et al. (2018). Oxidized iron in garnets from the mantle transition zone. *Nature Geoscience*, 11(2), 144–147.
- Kuritani, T., Xia, Q., Kimura, J., Liu, J., Shimizu, K., Ushikubo, T., et al. (2019). Buoyant hydrous mantle plume from the mantle transition zone. *Scientific Reports*, 9(1), 6549.
- Li, Z., Gerya, T., & Connolly, J. (2019). Variability of subducting slab morphologies in the mantle transition zone: Insight from petrological-thermomechanical modeling. *Earth-Science Reviews*, 196, 102874.
- Pearson, D., Brenker, F., Nestola, F., McNeill, J., Nasdala, L., Hutchison, M., et al. (2014). Hydrous mantle transition zone indicated by ringwoodite included within diamond. *Nature*, 507(7491), 221–224.
- Riel, N., Kaus, B., Green, E., & Berlie, N. (2022). MAGEMin, an efficient gibbs energy minimizer: Application to igneous systems. *Geochemistry, Geophysics, Geosystems*, 23(7), e2022GC010427.
- Ringwood, A. (1962). A model for the upper mantle. *Journal of Geophysical Research*, 67(2), 857–867.
- Ringwood, A. (1991). Phase transformations and their bearing on the constitution and dynamics of the mantle. *Geochimica Et Cosmochimica Acta*, 55(8), 2083–2110.
- Ringwood, A. E. (1975). Composition and petrology of the earth's mantle. *MacGraw-Hill*, 618.
- Schubert, G., Yuen, D., & Turcotte, D. (1975). Role of phase transitions in a dynamic mantle. *Geophysical Journal International*, 42(2), 705–735.
- Stixrude, L., & Lithgow-Bertelloni, C. (2012). Geophysics of chemical heterogeneity in the mantle. *Annual Review of Earth and Planetary Sciences*, 40, 569–595.
- Sun, S. (1982). Chemical composition and origin of the earth's primitive mantle. *Geochimica Et Cosmochimica Acta*, 46(2), 179–192.

- Sun, S., & McDonough, W. (1989). Chemical and isotopic systematics of oceanic basalts: Implications for mantle composition and processes. *Geological Society, London, Special Publications*, 42(1), 313–345.
- Wang, X., Wilde, S., Li, Q., & Yang, Y. (2015). Continental flood basalts derived from the hydrous mantle transition zone. *Nature Communications*, 6(1), 7700.
- Waszek, L., Tauzin, B., Schmerr, N., Ballmer, M., & Afonso, J. (2021). A poorly mixed mantle transition zone and its thermal state inferred from seismic waves. *Nature Geoscience*, 14(12), 949–955.
- Workman, R., & Hart, S. (2005). Major and trace element composition of the depleted MORB mantle (DMM). *Earth and Planetary Science Letters*, 231(1-2), 53–72.
- Yang, H., Kinzler, R., & Grove, T. (1996). Experiments and models of anhydrous, basaltic olivine-plagioclase-augite saturated melts from 0.001 to 10 kbar. *Contributions to Mineralogy and Petrology*, 124(1), 1–18.
- Yang, J., & Faccenda, M. (2020). Intraplate volcanism originating from upwelling hydrous mantle transition zone. *Nature*, 579(7797), 88–91.
- Yoshino, T., Manthilake, G., Matsuzaki, T., & Katsura, T. (2008). Dry mantle transition zone inferred from the conductivity of wadsleyite and ringwoodite. *Nature*, 451(7176), 326–329.
- Zhou, W., Hao, M., Zhang, J., Chen, B., Wang, R., & Schmandt, B. (2022). Constraining composition and temperature variations in the mantle transition zone. *Nature Communications*, 13(1), 1094.

4 Appendix

4.1 Gibbs Free Energy Minimization Benchmarking Results

Estimated bulk compositions for primitive and depleted mantle rocks (Table 1) were used for benchmarking GFEM programs [MAGEMin](#) and [Perple_X](#) (Connolly, 2009; Riel et al., 2022). Table 2 shows the computation times with respect to various PT grid resolutions (8x8, 16x16, 32x32, 64x64, 128x128). All computations were made on a Macbook Pro (2022; M2 chip) with macOS 13.4 and Python 3.11.4. Note that MAGEMin was ran on 6 CPU cores in parallel, while Perple_X does not have parallel capabilities.

Table 2: Computation times for various bulk mantle compositions.

Sample	PT Grid Size	MAGEMin (s)	Perple_X (s)	Perple_X/MAGEMin
DMM	64	1.9	17.1	9.0
NMORB	64	1.3	21.2	16.3
PUM	64	0.7	18.8	26.8

Sample	PT Grid Size	MAGEMin (s)	Perple_X (s)	Perple_X/MAGEMin
RE46	64	5.0	22.1	4.4
DMM	256	3.4	63.0	18.5
NMORB	256	3.9	79.1	20.2
PUM	256	2.0	65.3	32.6
RE46	256	15.0	82.2	5.4
DMM	1024	9.1	229.8	25.2
NMORB	1024	13.8	264.7	19.1
PUM	1024	7.7	245.2	31.8
RE46	1024	55.4	283.4	5.1
DMM	4096	33.0	847.4	25.7
NMORB	4096	54.9	995.9	18.1
PUM	4096	29.7	922.1	31.0
RE46	4096	201.8	1036.1	5.1
DMM	16384	128.9	3381.2	26.2
NMORB	16384	211.7	3827.6	18.1
PUM	16384	115.4	3672.7	31.8
RE46	16384	774.4	4102.7	5.3

5 Extra

Table 3: Ambient Mg-rich densities of mantle minerals (Stixrude & Lithgow-Bertelloni, 2012).

Mineral	Formula	Structure	Density (g/cm ³)	% transition
Plagioclase	(Ca, Na)(Al, Si) ₂ O ₈	Triclinic	2.69	0–10/0
Orthopyroxene	(Mg, Fe) ₂ Si ₂ O ₆	Monoclinic	3.20	0–20/0
Olivine	(Mg, Fe) ₂ SiO ₄	Orthorhombic	3.27	60–80/0
Clinopyroxene	(Mg, Fe, Ca)(Si, Al) ₂ O ₆	Monoclinic	3.40	0–18/0

Mineral	Formula	Structure	Density (g/cm ³)	% transition
Garnet	(Mg, Fe) ₃ Al ₂ Si ₃ O ₁₂	Cubic	3.58	0–40/0
Spinel	MgAl ₂ O ₄	Cubic	3.64	0–1/0
Ferropericlase	(Mg, Fe)O	Cubic	3.78	0/72–76
Wadsleyite	(Mg, Fe) ₂ SiO ₄	Orthorhombic	3.84	60–80/0
Ringwoodite	(Mg, Fe) ₂ SiO ₄	Cubic	3.90	60–80/0
Bridgmanite	(Mg, Fe)SiO ₃	Perovskite	4.10	0/18–22